Supporting Information

Dislocation Evolution and Migration at Grain Boundaries in Thermoelectric SnTe

Di Wu[†], Xiang Chen[‡], Fengshan Zheng[§,*], Hongchu Du[§,‖], Lei Jin[§,*], Rafal E. Dunin-Borkowski[§]

[†]Key Laboratory for Macromolecular Science of Shaanxi Province, Shaanxi Key Laboratory for Advanced Energy Devices, School of Materials Science and Engineering, Shaanxi Normal University, Xi'an 710119, China

[‡]Materials Chemistry, RWTH Aachen University, 52074 Aachen, Germany

[§]Ernst Ruska-Centre for Microscopy and Spectroscopy with Electrons and Peter Grünberg Institute, Forschungszentrum Jülich, 52425 Jülich, Germany

[‖]Central Facility for Electron Microscopy, RWTH Aachen University, 52074 Aachen, Germany

Sample Synthesis

Stoichiometric proportions of Sn shots (99.9%, Alfa Aesar), Te ingots (99.99%, Alfa Aesar) and In shots (99.99%, Alfa Aesar) of nominal composition $Sn_{0.995}In_{0.005}Te$ were evacuated (< 5×10^{-4} Pa) and sealed in quartz tubes. The following solid solution reaction recipe was used: the quartz tube was heated to 1000 °C over 12 hours and kept at this temperature for a further 12 hours, before being water quenched to room temperature. One piece of the resulting ingot was termed sample IAC in the text, while the other pieces were taken from the quartz tube, hand milled or ball milled (for 30 minutes in a SPEX-8000, US high energy ball miller) into powders for subsequent spark plasma sintering (Dr. Sinter, Japan) and marked HMS or BMS. The sintering process was carried out at 550 °C for 5 minutes under a uniaxial pressure of 50 MPa. The pellets were then cut into rectangular pieces of ~12×2×2 mm for electrical transport measurements, while coins of Φ ~10 mm and thickness ~1.5 mm were used for thermal diffusivity measurements.

Thermoelectric Property Characterization

Seebeck coefficients S and electrical conductivities σ were measured simultaneously in a commercial ZEM-3 (Ultravac, Japan) in an atmosphere of argon. The uncertainty of the measurements is estimated to be ~5% for each parameter. Thermal diffusivities D were measured in a state-of-the-art LFA 457 (Netzsch, Germany). Specific heats C_p were obtained according to the theoretical Dulong-Petit limit $3R/M$, where M is the average atomic mass per mol. Mass densities were measured using Archimedes' method. Thermal conductivities were calculated using the equation $\kappa = DC_p\rho$. Mass densities of

samples were measured using the Archimedes method in distilled water, and all found to be >98% theoretical value (6.48 g/cm^3), Table S1. Room temperature carrier concentrations were measured in a Lakeshore 8400 Hall measurement station using the van der Pauw method, Table S4. The samples were polished to be thinner than 1 mm for the measurements. The electrical thermal conductivity κ_e is related to σ *via* the Wiedemann-Franz law $\kappa_e = L\sigma T$, where the Lorenz constant L can be estimated from a measured Seebeck coefficient based on a simplified model[1].

Sound velocities (longitudinal and transverse) were measured at room temperature by the ultrasonic pulse-echo method with an Olympus 5073PR pulser/receiver. The results are listed in Table S2.

Table S1. Mass densities of the three samples IAC, HMS and BMS.

Sample	ρ (g/cm^3)	ρ / ρ_{theory}
IAC	6.397	98.7%
HMS	6.38	98.5%
BMS	6.35	98.0%

Table S2. Room temperature longitudinal and transverse sound velocities (v_l and v_t), as well as deduced phonon mean free paths (MFPs) of the IAC, HMS and BMS $Sn_{0.995}In_{0.005}Te$ samples.

Sample	v_l (m/s)	v_t (m/s)	v (m/s)	*MFPs* (nm)
IAC	3120	1380	1695	6.198
HMS	3150	1330	1647	4.994
BMS	2885	1210	1500	4.292

X-ray Diffraction Characterization

Powder X-ray diffraction (XRD) patterns were taken under a Smartlab (9 kW, Rigaku, Japan) equipment.

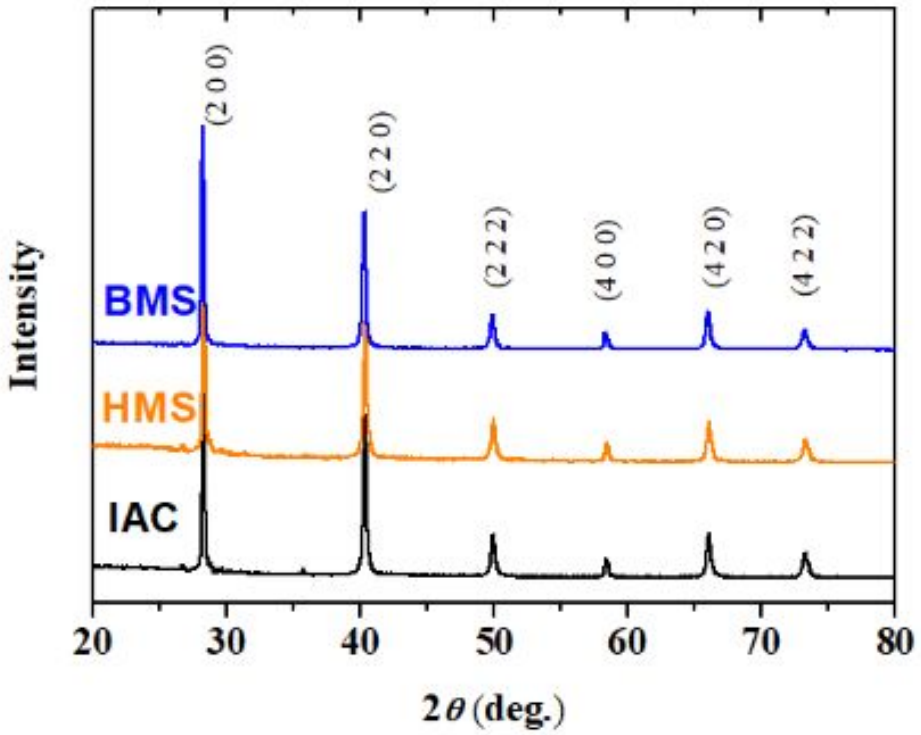

Figure S1. X-ray diffraction patterns of the three samples IAC (black), HMS (orange) and BMS (blue) showing that all samples are phase pure.

Electron Back Scattered Diffraction (EBSD) Characterization

The EBSD characterizations (Fig. S2) were carried out to systematically investigate the grain size distribution and crystallographic orientation for more reliable statistics in each sample. The samples for EBSD investigations were grinded with SiC papers (1200 grid), and mechanically polished with 3 μm and 1 μm diamond suspensions (Struers, Germany). The EBSD experiments were carried out on an FEI Helios NanoLab™ 660 scanning electron microscope equipped with a thermal field-emission gun operated at 30 kV and a beam current of 1.6 nA. The EBSD patterns were collected pixel-by-pixel across an area using a pixel size of 0.1 μm. EBSD analysis was performed using EDAX OIM™ Analysis 8 software.

For the IAC sample, we present the EBSD results in Fig. S2(a) and Fig. S2(b), because the grain size is apparently not homogeneous. Nevertheless, it can be seen that even for the area including mainly the small grains shown in Fig. S2(a) has a much larger average size than in the HMS and BMS samples, as evidenced by Fig. S2(b)-(d). The average grain size is about 4.72, 1.05 and 0.68 μm for the IAC, HMS and BMS samples, respectively, in accordance with the TEM results.

According to the EBSD results, the following aspects are deduced:

i) The grain size in the IAC sample is the largest, due to homogeneous annealing treatment without subsequent milling.

ii) The grain size in the HMS and BMS samples processed by milling + SPS are finer than in the IAC samples, due to the different levels of plastic strains applied in the hand/ball milling process.

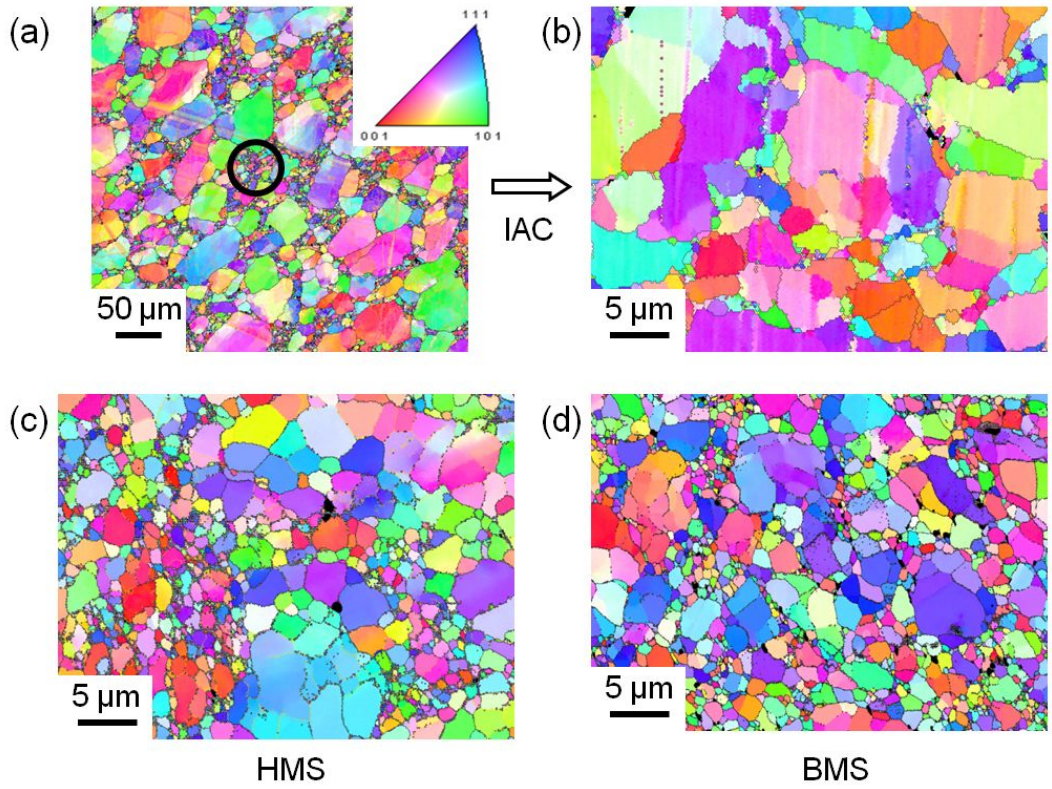

Figure S2 EBSD mapping for the (a, b) IAC, (c) HMS and (d) BMS samples, respectively. The orientation is color coded according to the legend triangle shown in (a). (b) Magnification of (a), showing areas with small grains (e.g., marked by circle) that cannot be well resolved in (a). For direct comparison, the scale bar in (b) to (d) is identical. The average grain size is about 4.72, 1.82, 1.05 and 0.68 μm for (a) to (d), respectively.

Transmission electron microscopy (TEM) Characterization

Samples for microstructural characterizations were prepared by standard mechanical grinding, polishing to a thickness of ~30 μm and Ar ion milling. Samples prepared by focused ion beam milling were performed on an FEI Helios Nanolab 400s dual-beam system[2]. TEM experiments were carried out in an FEI Tecnai transmission electron microscope at 200 kV. STEM experiments were carried out in an FEI Titan ChemiSTEM G[2] 80-200 transmission electron microscope at 200 kV[3]. The convergence semi-angle and collection semi-angle for STEM LAADF and HAADF imaging were 25 mrad, 30-70 mrad and 70-200 mrad, respectively. Strain analysis of STEM HAADF images was carried out using the home-written geometric phase analysis software.

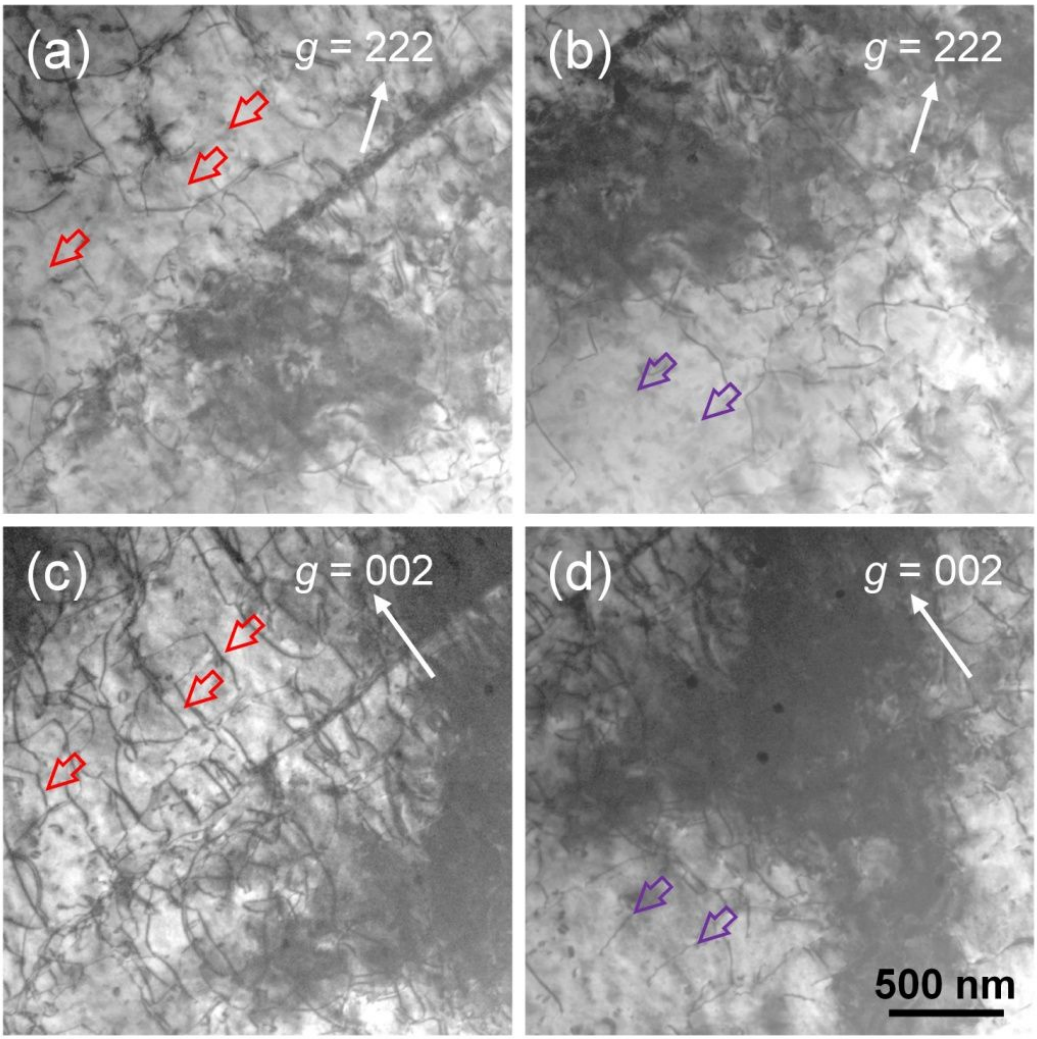

Figure S3. Low magnification TEM images from a single grain of the IAC sample showing a high density of in-grain dislocations. The Burgers vector was found to be *a*<110> type on the basis of the $\boldsymbol{g}\cdot\boldsymbol{b}=0$ criterion ($\boldsymbol{g}$: reciprocal lattice vector, $\boldsymbol{b}$: Burgers vector), with g = 222 in (a)-(b) and g = 002 in (c)-(d) for two areas. Scale bar is the same for all images. The red and purple arrows show the extinction and presence of dislocation contrast.

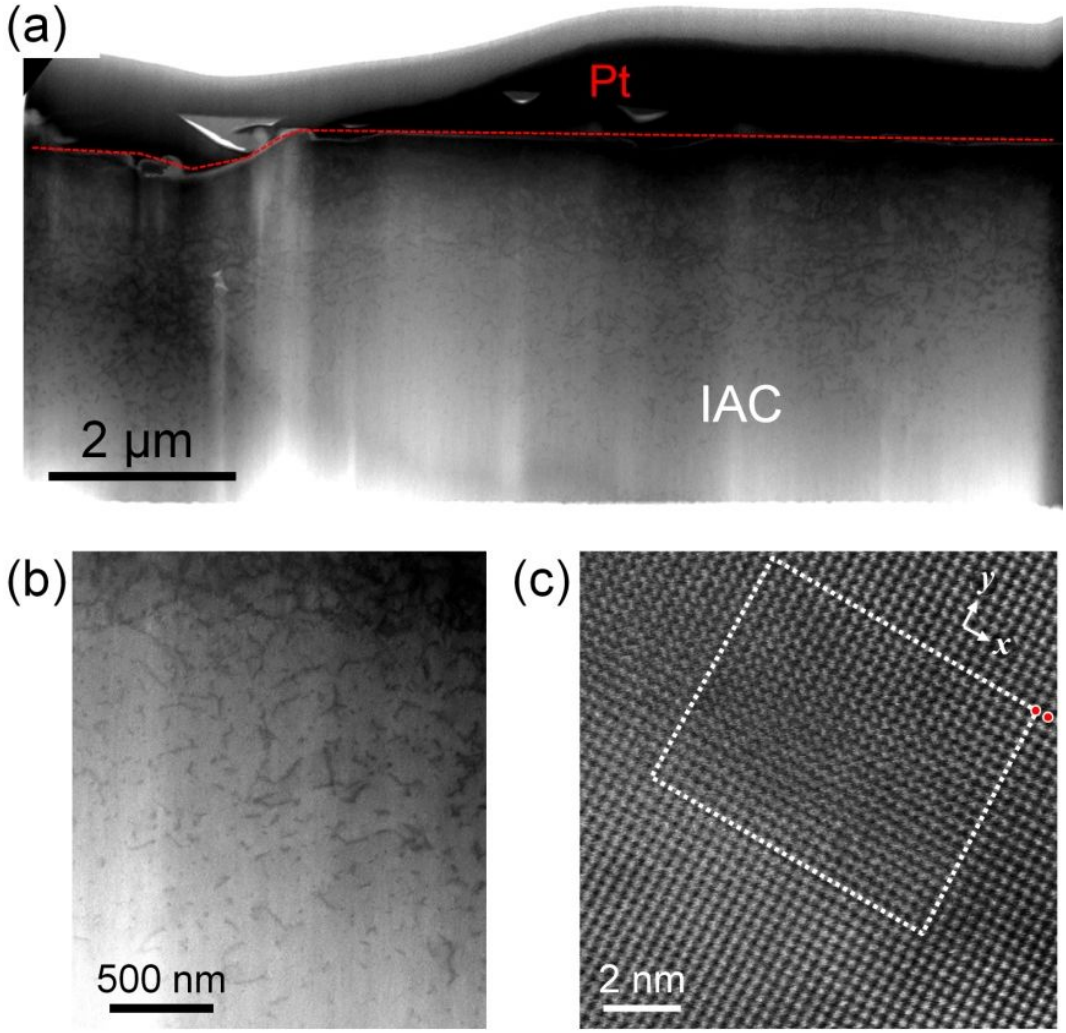

Figure S4. (a) and (b) Low-magnification BF STEM images from a single grain of the IAC sample showing a high density of in-grain dislocations. The sample was prepared by focused-ion beam milling. (c) High-resolution HAADF STEM image showing the presence of dislocations. Burgers circuit analysis showing a projected Burgers vector of $-a/2$ [100]. Taking the dislocation component along the viewing direction into account, the Burgers vector is $a/2$ [-101] or $-a/2$ [101].

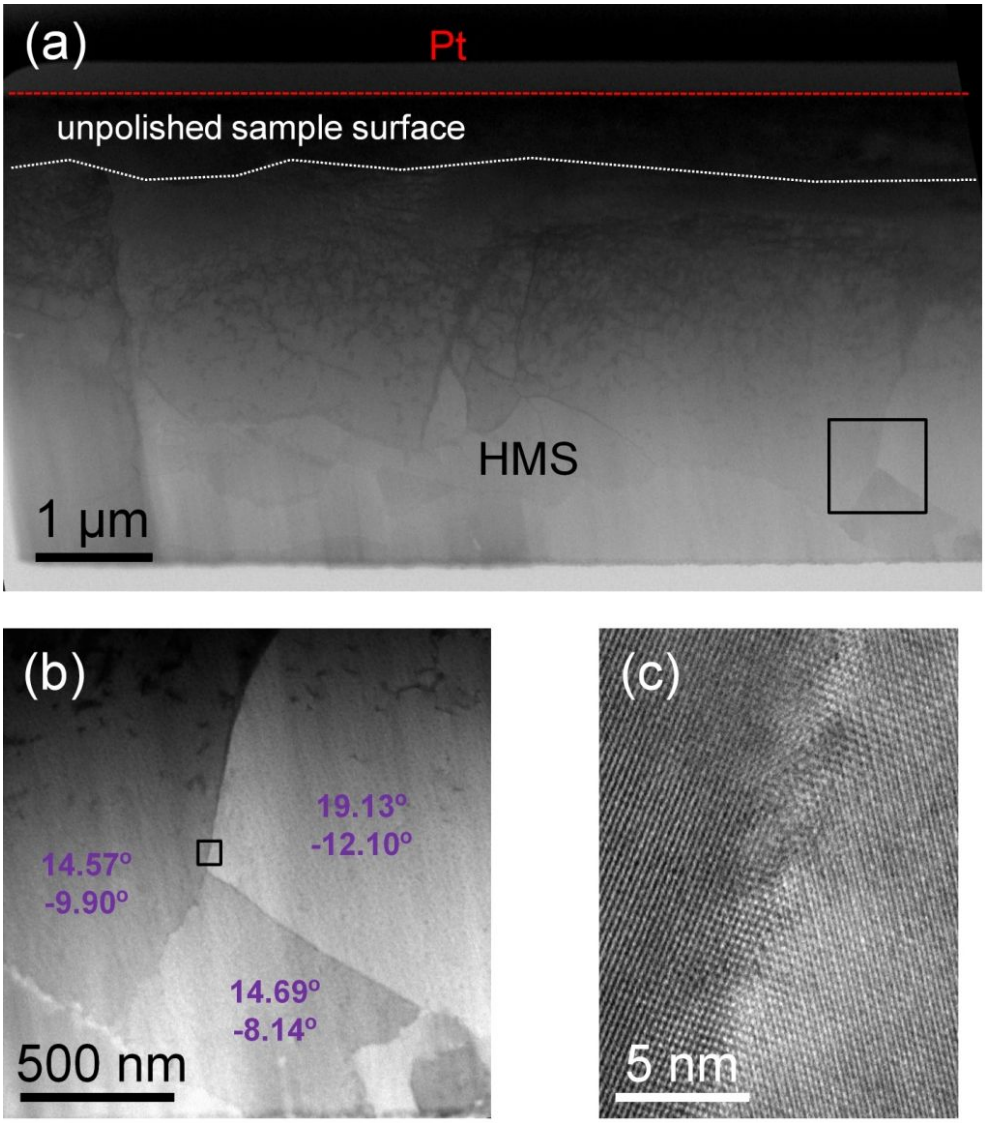

Figure S5. (a) Low-magnification BF STEM image taken from the HMS sample. The sample was prepared by focused-ion beam milling. Relatively large grains with size of about 3 μm are present close to the unpolished surface, together with small grains with a size of about 1 μm. The observation is consistent with the EBSD result shown in Fig. S2(c). (b) Magnification of a triple grain boundary area shown in (a), as marked by the rectangle. The alpha and beta angles of zone axes for each grain are shown in (b), leading to a difficulty in imaging the grains with atomic resolution simultaneously. (c) High-resolution HAADF STEM image taken from the indicated area in (b), showing the grain boundary. The sample tilt is 16.09º, -12.10º, which is slightly away from both grains nearby.

Repeatability of electrical performance of IAC sample

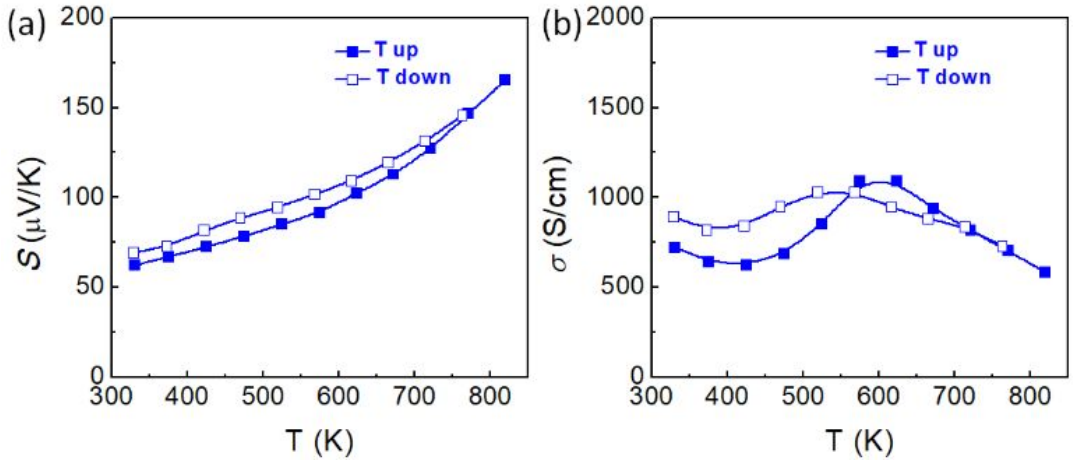

Figure S6. (a) Seebeck coefficient and (b) electrical conductivity for the IAC sample in an entire measuring cycle.

Lattice thermal conductivity simulation via Debye-Callaway model

The lattice thermal conductivity κ_{lat} can be written in the form

$$\kappa_{lat} = \frac{k_B}{2\pi^2 v}\left(\frac{k_B T}{\hbar}\right)^3 \int_0^{\theta_D/T} \tau_c \frac{\varsigma^4 e^{\varsigma}}{(e^{\varsigma}-1)^2} d\varsigma \quad (1)$$

Individual scattering mechanisms contribute to the total relaxation time τ_c according to *Matthiessen*'s rule:

$$\tau_c = (\tau_U^{-1} + \tau_N^{-1} + \tau_{GB}^{-1} + \tau_v^{-1})^{-1} \quad (2)$$

Where Umklapp process[4]

$$\tau_U^{-1} \approx \frac{\hbar\gamma^2}{Mv^2\theta_D}\omega^2 T \exp(-\frac{\theta_D}{3T}) \quad (3)$$

Normal process[5]

$$\tau_N^{-1} \approx \beta\tau_U^{-1} \quad (4)$$

Grain boundary scattering

$$\tau_{GB}^{-1} = vD \quad (5)$$

Vacancy scattering[6,7]

$$\tau_v^{-1} = \frac{\omega^4\delta^3}{4\pi v^3} x(1-x)\left[-\frac{M_v}{M} - 2\right]^2 \quad (6)$$

k_B is Boltzmann's constant, h is Planck's constant, v is the bulk sound (phonon-group) velocity, θ_D is the bulk Debye temperature, ς is defined as $h\omega/k_BT$, γ is the *Grüneisen* parameter, M is the average molar mass of one atom, ΔM is the mass difference between impurity and host atoms; β is a fitting parameter for the Normal process; D is the grain boundary density, δ is the average radius of a primitive cell, x is the molar ratio of Sn vacancies deduced from the carrier concentration, and M_v is the molar mass of the missing atom (vacancy).

Table S3. Parameters used in the simulations of lattice thermal conductivity.

	θ_D (K)	165	Ref.[8,9]
	β	1.2	fitted
	v (m/s)	1800	Ref.[9]
	M (g/mol)	246.31	-
	M_v (g/mol)	118.71	-
	γ	1.75	calculated[10,11]
	δ (nm)	0.199	calculated[9]
IAC	x	0.0202	deduced from p[&]
	D (μm^{-1})	0.1	TEM statistics
HMS	x	0.0148	deduced from p[&]
	D (μm^{-1})	0.7	TEM statistics
BMS	x	0.0218	deduced from p[&]
	D (μm^{-1})	2.2	TEM statistics

[&] The molar ratio of Sn vacancies can be deduced from the measured hole concentration, on the basis of the known volume of the SnTe primitive cell = 63.049 Å^3 in Ref.[9]

Table S4. Room temperature Hall carrier concentrations p and mobilities μ of the IAC, HMS and BMS $Sn_{0.995}In_{0.005}Te$ samples.

Sample	p ($10^{20}/cm^3$)	μ (cm^2/Vs)
IAC	6.4	7.1
HMS	4.7	47.0
BMS	6.9	56.4

References

(1) Kim, H. S.; Liu, W.; Chen, G.; Chu, C. W.; Ren, Z. Relationship between Thermoelectric Figure of Merit and Energy Conversion Efficiency *Proc. Natl. Acad. Sci. U S A* **2015**, *112*, 8205-8210.

(2) Ernst Ruska-Centre for Microscopy and Spectroscopy with Electrons. FEI Helios NanoLab 400S FIB-SEM. *JLSRF* **2016**, *2*, A40.

(3) Ernst Ruska-Centre for Microscopy and Spectroscopy with Electrons. FEI Titan G^2 80-200 Crewley *JLSRF* **2016**, *2*, A43.

(4) Morelli, D.; Heremans, J.; Slack, G. Estimation of the Isotope Effect on the Lattice Thermal Conductivity of Group IV and Group III-V Semiconductors *Phys. Rev. B* **2002**, *66*, 195304.

(5) He, J.; Girard, S. N.; Kanatzidis, M. G.; Dravid, V. P. Microstructure-Lattice Thermal Conductivity Correlation in Nanostructured $PbTe_{0.7}S_{0.3}$ thermoelectric Materials *Adv. Funct. Mater.* **2010**, *20*, 764-772.

(6) Klemens, P. Theory of Thermal Conduction in Thin Ceramic Films *Int. J. Thermophys.* **2001**, *22*, 265-275.

(7) Klemens, P. G. Phonon Scattering by Oxygen Vacancies in Ceramics *Physica B: Condensed Matter.* **1999**, *263*, 102-104.

(8) Gaur, U.; Pultz, G.; Wiedemeier, H.; Wuderlich, B. Analysis of the Heat Capacities of Group IV Chalcogenides Using Debye Temperatures *J. Therm.Anal.* **1981**, *21*, 309-326.

(9) Bauer Pereira, P.; Sergueev, I.; Gorsse, S.; Dadda, J.; Müller, E.; Hermann, R. P. Lattice Dynamics and Structure of GeTe, SnTe and PbTe *Phys. Status Solidi* B **2013**, *250*, 1300-1307.

(10) Pei, Y.; Zheng, L.; Li, W.; Lin, S.; Chen, Z.; Wang, Y.; Xu, X.; Yu, H.; Chen, Y.; Ge, B. Interstitial Point Defect Scattering Contributing to High Thermoelectric Performance in SnTe *Adv. Electron. Mater.* **2016**, *2*, 1600019.

(11) Xiao, Y.; Chang, C.; Pei, Y.; Wu, D.; Peng, K.; Zhou, X.; Gong, S.; He, J.; Zhang, Y.; Zeng, Z.; Zhao, L.-D. Origin of Low Thermal Conductivity in SnSe *Phys. Rev. B* **2016**, *94*, 125203.